Investigating the effects of the change in the angle of attack on the Mack mode frequencies in a Mach 6 wind tunnel on a slender cone

Arkin Idnani*
University of Maryland, College Park, MD 20742

An experimental investigation is conducted to examine the influence of angle of attack on the Mack mode (second-mode) instability over a slender cone immersed in a hypersonic flow. Experiments are performed in the University of Maryland HyperTERP Ludwieg tube facility at a nominal freestream Mach number of 6.2 using a 5° half-angle cone.
The angle of attack is varied between $-3°$ and $+5°$, with schlieren-based spectral measurements obtained in the range $-1°$ to $+2°$. Z-type schlieren imaging combined with high-speed visualization at 800,000 frames per second is used to capture the boundary-layer disturbance field on the upper surface of the cone.
At zero incidence, a clear second-mode spectral peak is identified at approximately 300 kHz. At $-1°$ angle of attack, where the upper surface becomes the windward side and the boundary layer is compressed, a visible increase in second-mode frequency is observed, consistent with boundary-layer thinning on the windward surface. At positive angles of attack, where the upper surface is leeward and the boundary layer thickens, no distinct second-mode peak is identifiable in the spectra.

Nomenclature

δ	=	boundary-layer thickness
f	=	frequency
f_0	=	second-mode fundamental (most-amplified) frequency
F	=	dimensionless frequency, $2\pi f/(U_\infty \cdot Re/m)$
M	=	Mach number
N	=	N factor (integrated spatial amplification rate)
p_0	=	reservoir stagnation pressure
R	=	stability Reynolds number, $\sqrt{Re_s}$
Re	=	Reynolds number based on freestream conditions and surface coordinate
Re/m	=	unit Reynolds number
s	=	streamwise surface coordinate
T_0	=	reservoir stagnation temperature
U_∞	=	freestream velocity
PSD	=	power spectral density

Subscripts

0	=	stagnation conditions
∞	=	freestream conditions
w	=	wall conditions

I. Introduction

The laminar-to-turbulent transition of hypersonic boundary layers is a problem of significant practical importance for the design of high-speed vehicles. Transition strongly influences surface heating rates and skin friction, both of which drive structural and thermal protection system sizing. Accurate prediction of transition onset therefore remains a central challenge in hypersonic aerodynamics.

*Undergraduate Researcher, Department of Aerospace Engineering, 3181 Glenn L. Martin Hall, College Park, MD 20742. Student Member AIAA.

For slender, axisymmetric bodies at zero incidence in a hypersonic freestream, the dominant transition mechanism is the Mack or second-mode instability [1]. These disturbances can be physically interpreted as acoustic waves trapped within the boundary layer, propagating at approximately 85–90% of the boundary-layer edge velocity. They are primarily two-dimensional in character and exhibit fundamental frequencies that scale inversely with boundary-layer thickness, ranging from tens of kilohertz to over a megahertz depending on the flow conditions [1]. Because of their large amplitude and strong density-gradient signature, second-mode waves are well suited to optical measurement techniques such as schlieren photography [2, 3].

In practice, hypersonic vehicles rarely fly at zero incidence. The introduction of an angle of attack breaks the azimuthal symmetry of the flow, creating a compressed, thinner boundary layer on the windward side and a thicker boundary layer on the leeward side. Since the second-mode fundamental frequency scales approximately as the inverse of the boundary-layer thickness, angle of attack is expected to shift instability frequencies upward on the windward surface and downward on the leeward surface relative to the zero-incidence case. Characterizing this effect is important for transition prediction hypersonic flight vehicles.

Prior experimental work has examined the effect of angle of attack on second-mode instability. Stetson and Kimmel [4] performed measurements on a 7° half-angle cone at Mach 8, finding a modest increase in second-mode amplification rate on the windward meridian with increasing angle of attack. Kennedy et al. [5, 6] extended this to Mach 14 using calibrated high-speed schlieren visualizations on the windward surface, finding slightly increased growth rates and additionally characterizing nonlinear harmonic interactions through bispectral analysis. Kennedy et al. [7] later examined both sharp and blunt 7° cones at Mach 6 in the Air Force Research Laboratory Ludwieg tube, finding good agreement between schlieren-derived N factors and parabolized stability equation (PSE) computations for the sharp-nose cases. However, none of these studies employed a 5° half-angle cone geometry, and the influence of angle of attack at Mach 6 conditions using the University of Maryland HyperTERP facility has not previously been reported.

In the present work, high-speed schlieren visualizations are used to investigate the effect of angle of attack on second-mode instability development over a 5° half-angle slender cone in the HyperTERP Ludwieg tube at a freestream Mach number of 6.2. Experiments are conducted at a single unit Reynolds number condition with the cone angle of attack varied between −3° and +5°. All measurements are made on the upper surface of the cone, which is the windward surface at negative angle of attack and the leeward surface at positive angle of attack. Power spectral density analysis of the schlieren time signals is used to identify the most-amplified second-mode frequencies as a function of angle of attack, and results are interpreted in the context of boundary-layer thickness changes induced by incidence.

II. Experimental Setup

A. Facility

All experiments were carried out in the HyperTERP Ludwieg tube at the University of Maryland. HyperTERP is an impulse facility that produces a short-duration steady test flow by releasing a pressurized gas column through a piston into a converging–diverging nozzle. For the conditions used in the present study, the driver section was charged to a stagnation pressure of $p_0 = 15$ bar at a stagnation temperature of $T_0 = 550$ K, producing a nominal freestream Mach number of $M_\infty = 6.2$. Each run produces a usable steady-flow test period of approximately 100 ms, which was sufficient to acquire the image sequences analyzed in this study.

B. Model

The test article is a 5° half-angle slender cone with a nominally sharp nose tip. The model was mounted at a fixed angle of attack for each individual run, with a separate run performed at each condition examined. Positive angle of attack is defined as the nose pitching upward. All schlieren visualizations were obtained from the upper surface of the cone, which corresponds to the leeward side at positive angle of attack and the windward side at negative angle of attack. The full range of angles of attack tested spans −3° to +5°; however, meaningful second-mode spectral measurements were obtained only in the range −1° to +2°, for reasons discussed in Section III.

C. Schlieren Visualization

A conventional Z-type schlieren system was used to visualize density gradients in the boundary layer. Illumination was provided by a continuous LED light source. A vertical knife-edge cutoff oriented perpendicular to the facility floor was used to visualize density gradients in the wall-normal direction. Images were recorded with a high-speed camera

operating at a frame rate of f_s = 800,000 frames per second, giving a Nyquist frequency of f_{Nyq} = 400 kHz. The field of view corresponded to the mid-section of the cone.

The image scale was determined by imaging a reference object of known physical size placed at the measurement plane. A quarter-inch (6.35 mm) screw was measured to span 101 pixels in the image, yielding a calibration factor of $6.35/101 \approx 0.063$ mm/pixel. The calibration image is shown in Fig. 1.

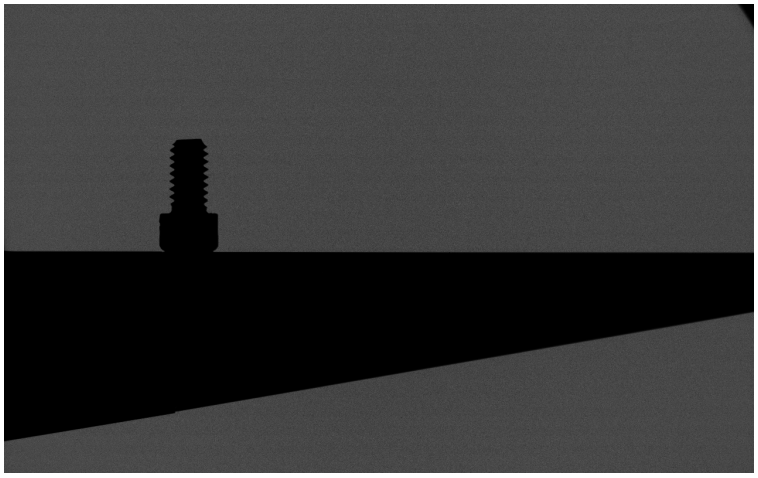

Fig. 1 Calibration image used to determine the image scale. A quarter-inch (6.35 mm) screw spans 101 pixels, yielding a scale of approximately 0.063 mm/pixel.

Raw schlieren images were loaded directly as grayscale intensity arrays. No background subtraction was applied; instead, a linear trend was removed from each extracted time series using MATLAB's `detrend` function prior to spectral estimation, suppressing low-frequency drift without altering the spectral content in the second-mode frequency range of interest. Example schlieren images from selected angle-of-attack conditions are shown in Fig. 2.

D. Data Reduction and Spectral Analysis

Spectral analysis was performed in MATLAB on the full image sequence acquired during each run, which consisted of approximately 4,000–5,000 frames per shot at 800 kHz.

For each angle-of-attack condition, a single wall-normal pixel row was selected within the boundary layer. The row was chosen manually based on visual inspection of the schlieren images to coincide with the region of maximum disturbance contrast, and varied between approximately $y = 17$ and $y = 45$ pixels from the cone surface depending on the angle of attack.

At each streamwise location, a spatial region of interest (ROI) was defined as a strip of variable width Δx centered on the chosen streamwise position, spanning the selected wall-normal row. The strip width was adjusted per condition based on visual inspection to optimize the signal-to-noise ratio of the extracted time series. Pixel intensities within each ROI were spatially averaged to produce a single scalar time series $S(t)$, suppressing pixel-level noise while retaining the temporal content associated with convecting boundary-layer disturbances. A linear trend was removed from each time series prior to spectral estimation.

Power spectral density estimates were computed using Welch's method with a Hann window and 50% overlap between segments, at a sampling frequency of f_s = 800 kHz. Spectra are reported in decibels as $10 \log_{10}$ of the one-sided PSD. A moving-mean smoothing filter with a window of 4 frequency bins was subsequently applied to aid visual identification of broadband spectral peaks. Both the raw and smoothed spectra were examined when identifying the dominant frequency at each condition.

III. Results and Discussion

A. Schlieren Visualizations

Figure 2 shows representative schlieren images from the upper surface of the cone at selected angles of attack. At 0°, rope-like disturbance structures characteristic of second-mode wavepackets are visible within the boundary layer as alternating dark and bright bands inclined at a shallow angle to the cone surface, consistent with the two-dimensional acoustic wave character of second-mode instability reported in prior literature [3, 5]. At −1°, where the upper surface is windward, the boundary layer appears visually compressed relative to the zero-incidence case, and disturbance structures with a shorter apparent spatial wavelength are visible, qualitatively consistent with a higher instability frequency. At positive angles of attack, the upper surface is leeward and the boundary layer thickens visibly; disturbance structures become less distinct and no clear wavepacket signature is identifiable.

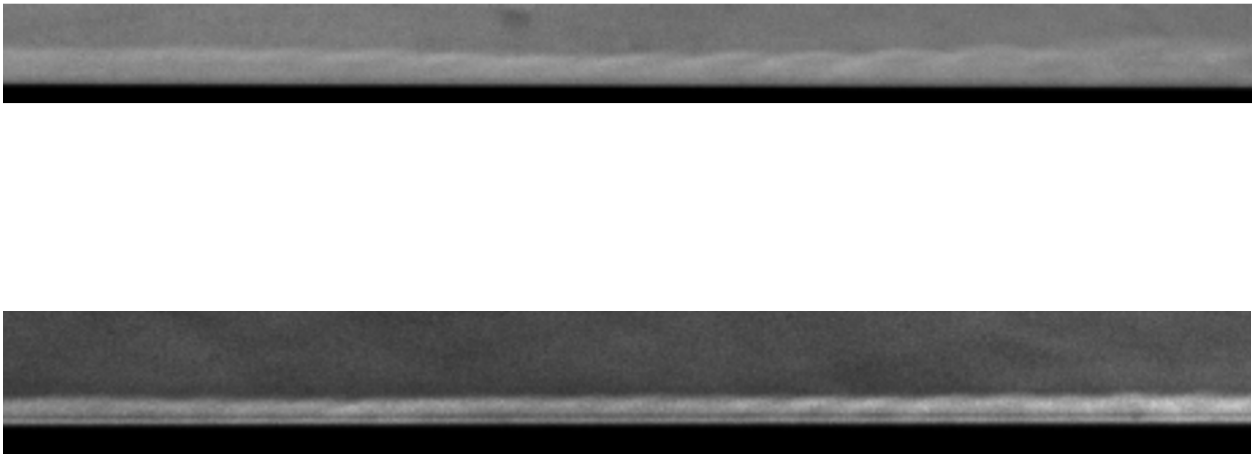

Fig. 2 Schlieren visualizations of the upper surface boundary layer at (top) 0° and (bottom) −1° angle of attack. At 0°, rope-like second-mode wavepacket structures are clearly visible. At −1° the upper surface is windward and the boundary layer is compressed, with disturbance structures exhibiting a shorter apparent spatial wavelength.

B. Spectral Analysis

1. Zero Angle of Attack

Power spectral density estimates at 0° angle of attack are presented in Fig. 3. Signals were extracted at the wall-normal location of maximum disturbance contrast, with consistent spectral signatures obtained across rows y = 19–21 px, of which the result at y = 20 px is shown as representative. A broad but consistent spectral peak near $f_0 \approx 300$ kHz is identifiable across all three rows in both the raw and smoothed spectra, providing confidence that this feature is physical rather than a noise artifact. This peak is interpreted as the most-amplified second-mode fundamental frequency at this condition.

2. Negative Angle of Attack (−1°)

PSD estimates at −1° angle of attack are presented in Fig. 4. At this condition the upper surface is windward and the boundary layer is visually compressed relative to the zero-incidence case. Signals were extracted at the wall-normal location of maximum disturbance contrast, which produced the most clearly defined spectral features. The smoothed spectra at these locations show a distinct hump at frequencies above the 0° peak, with spectral energy increasing toward

and approaching the 400 kHz Nyquist limit of the imaging system. The apparent shift of the dominant spectral feature to higher frequencies relative to the zero-incidence case is consistent with boundary-layer compression on the windward surface: a thinner boundary layer supports higher-frequency second-mode instabilities via the scaling $f_0 \sim U_e/(2\delta)$ [1].

It is noted that the absolute power levels at $-1°$ are elevated by approximately 10–15 dB relative to the $0°$ case. This is attributed to run-to-run variability in schlieren system illumination rather than a physical increase in disturbance amplitude, since no normalization between runs was applied. The frequency shift itself remains a physically interpretable result independent of the absolute power level. Because the dominant spectral feature approaches the Nyquist limit, a precise peak frequency cannot be extracted; the observed shift should therefore be interpreted as a lower bound on the true frequency increase.

3. Positive Angles of Attack (+1° and +2°)

PSD estimates at +1° and +2° angle of attack are presented in Fig. 5. At these conditions the upper surface is leeward and the boundary layer thickens visibly relative to the zero-incidence case. No distinct spectral peak is identifiable at any of the streamwise locations examined; the PSD estimates decay monotonically without a discernible hump above the noise floor. The leeward boundary-layer thickening with increasing positive angle of attack would be expected to shift the second-mode frequency to lower values and reduce the instability growth rate relative to zero incidence, consistent with the absence of a resolvable spectral peak at these conditions.

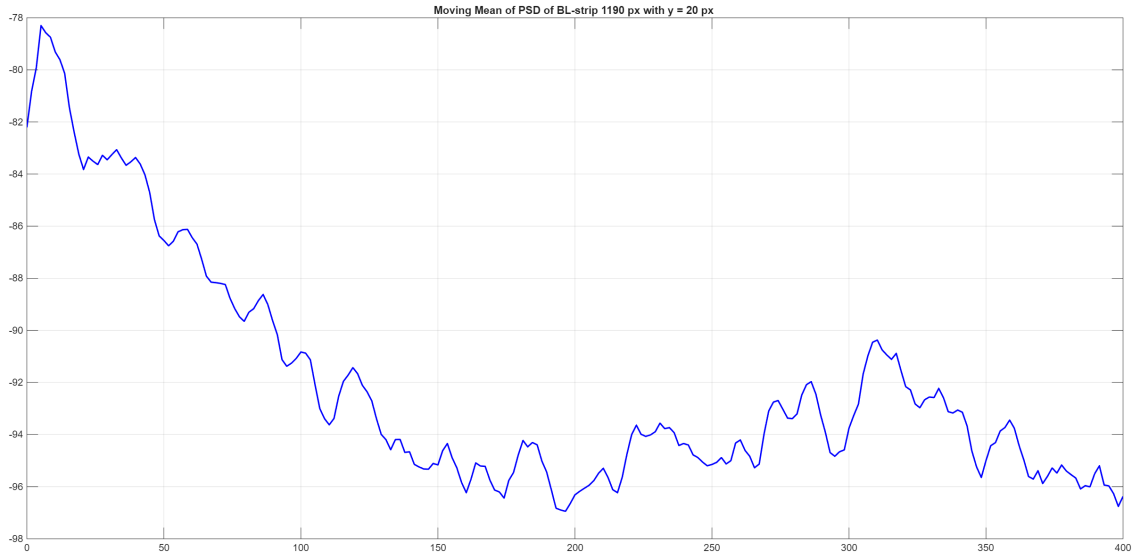

Fig. 3 Power spectral density estimates at $0°$ angle of attack averaged across five streamwise locations. A broadband second-mode peak near $f_0 \approx 300$ kHz is consistently identifiable in the spectra.

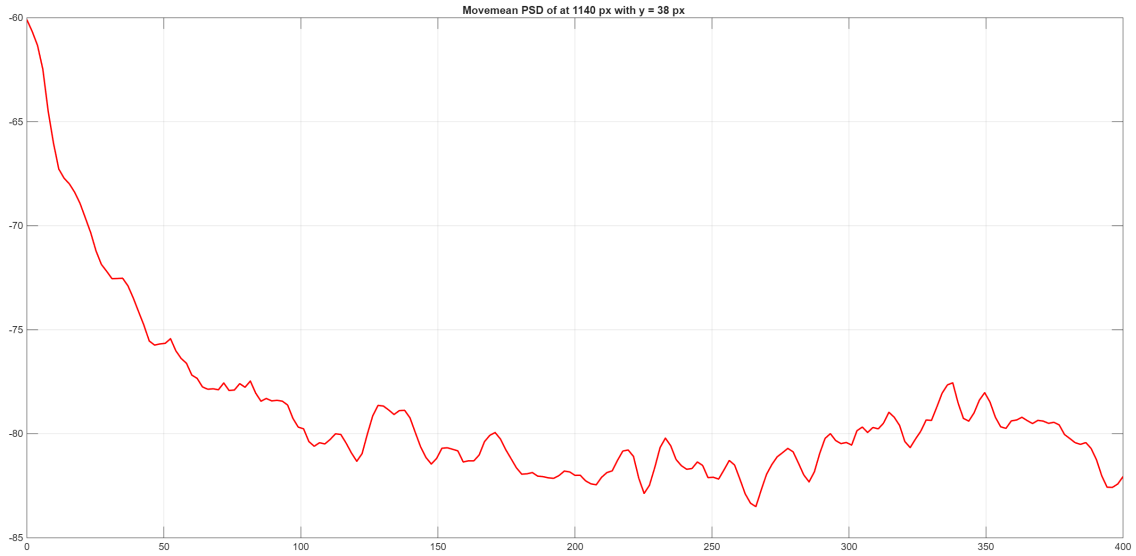

Fig. 4 Power spectral density estimates at $-1°$ angle of attack averaged across three streamwise locations. The upper surface is windward at this condition; spectral activity increases toward higher frequencies relative to the $0°$ case, consistent with boundary-layer compression on the windward surface.

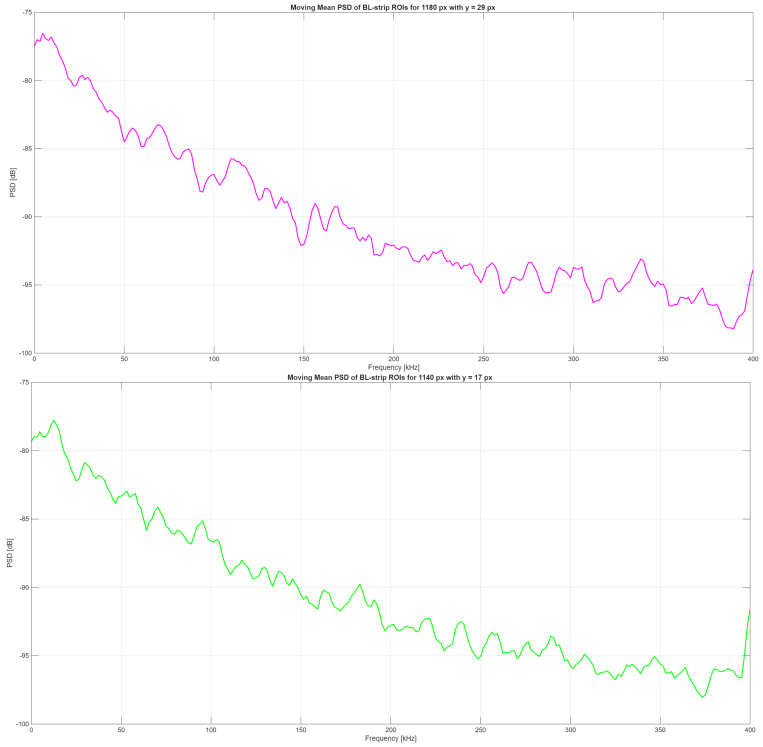

Fig. 5 Power spectral density estimates at (top) $+1°$ and (bottom) $+2°$ angle of attack. The upper surface is leeward at these conditions. No distinct second-mode peak is identifiable; spectra decay monotonically without a discernible hump above the noise floor.

C. Effect of Angle of Attack on Second-Mode Frequency

The spectral results across all conditions are consistent with the expected physical behavior of the second-mode instability under angle-of-attack effects. At zero incidence a clear peak near $f_0 \approx 300$ kHz is established as a baseline. At $-1°$, where the imaged surface is windward and the boundary layer is compressed, the dominant spectral feature shifts to higher frequencies, approaching the measurement bandwidth limit. At positive angles of attack, where the imaged surface is leeward and the boundary layer thickens, no peak is resolved.

The present observations are qualitatively consistent with prior experimental work. Kennedy et al. [5, 6] and Stetson and Kimmel [4] both reported increased second-mode frequencies and growth rates on the windward surface with increasing (negative) angle of attack on 7° half-angle cones at Mach 14 and Mach 8 respectively. The present results extend this picture to a 5° half-angle geometry at Mach 6.2 in the HyperTERP facility, albeit at a qualitative level.

The measurements are qualitative in nature. Future work should include PSE stability calculations for the 5° cone at the present flow conditions, an increase in camera frame rate to extend the measurable bandwidth beyond 400 kHz, and simultaneous measurements on both surfaces to allow a complete characterization of the windward–leeward asymmetry induced by angle of attack.

Acknowledgments

The author gratefully acknowledges Professor Stuart J. Laurence for his guidance and support throughout this research, which was conducted as part of an Honors Thesis at the University of Maryland. The author also thanks Dr. Antonios Gementzopoulos for his technical expertise and many helpful discussions during the course of the research project.

References

[1] Mack, L. M., "Linear stability theory and the problem of supersonic boundary-layer transition," *AIAA Journal*, Vol. 13, No. 2, 1975, pp. 278–289.

[2] Laurence, S. J., Wagner, A., and Hannemann, K., "Schlieren-based techniques for investigating instability development and transition in a hypersonic boundary layer," *Experiments in Fluids*, Vol. 55, No. 8, 2014, pp. 1–17.

[3] Laurence, S. J., Wagner, A., and Hannemann, K., "Experimental study of instability growth and breakdown in a hypersonic boundary layer using high-speed schlieren visualization," *Journal of Fluid Mechanics*, Vol. 797, 2016, pp. 471–503.

[4] Stetson, K. F., and Kimmel, R. L., "On Hypersonic Boundary-Layer Stability," *30th AIAA Aerospace Sciences Meeting*, 1992.

[5] Kennedy, R. E., Laurence, S. J., Smith, M. S., and Marineau, E. C., "Investigation of the second-mode instability at Mach 14 using calibrated schlieren," *Journal of Fluid Mechanics*, Vol. 845, 2018, p. R2.

[6] Kennedy, R. E., Laurence, S. J., Smith, M. S., and Marineau, E. C., "Visualization of the Second-Mode Instability on a Sharp Cone at Mach 14," *2018 AIAA Aerospace Sciences Meeting*, 2018.

[7] Kennedy, R. E., Jewell, J. S., Paredes, P., and Laurence, S. J., "Characterization of instability mechanisms on sharp and blunt slender cones at Mach 6," *Journal of Fluid Mechanics*, Vol. 936, 2022, p. A39.